

Phase evolution and kinetics of the oxidation of monosulfide solid solution under isothermal conditions

Haipeng Wang^{a,*}, Allan Pring^{b,c}, Yaning Xie^d, Yung Ngothai^a, Brian O'Neill^a

^a School of Chemical Engineering, University of Adelaide, SA 5005, Australia

^b Department of Mineralogy, South Australian Museum, SA 5001, Australia

^c School of Earth and Environmental Science, University of Adelaide, SA 5005, Australia

^d Beijing Synchrotron Radiation Laboratory, Institute of High Energy Physics, Beijing 100039, PR China

Received 18 June 2004; received in revised form 31 July 2004; accepted 6 August 2004

Available online 15 September 2004

Abstract

In this work, the effects of stoichiometry on phase evolution during the oxidation of *mss* (monosulfide solid solution) were investigated. A series of *mss* samples, ranging from $\text{Fe}_{7.9}\text{S}_8$ to $\text{Fe}_{2.37}\text{Ni}_{5.53}\text{S}_8$ were synthesized from pure components. Samples with grain size 53–90 μm were oxidized at 830 and 850 K in air in a muffle furnace. The *Rietveld* quantitative phase analysis method was used to identify and quantify the phase information from powder X-ray diffraction (XRD) profiles.

Hematite was observed and accounted for most of the oxidized iron. Nickel in *mss* was not oxidized to NiO under current isothermal conditions; instead, it was finally transformed to $\text{Ni}_{17}\text{S}_{18}$. Hematite, $\text{Fe}_2(\text{SO}_4)_3$ and residual *mss* were identified in the final phases after 24 h oxidation of the *mss* composition $\text{Fe}_{7.9}\text{S}_8$; hematite and $\text{Ni}_{17}\text{S}_{18}$ for compositions $\text{Fe}_{6.15}\text{Ni}_{1.54}\text{S}_8$ and $\text{Fe}_{2.37}\text{Ni}_{5.53}\text{S}_8$; hematite, $\text{Ni}_{17}\text{S}_{18}$ and pentlandite for $\text{Fe}_{6.4}\text{Ni}_{1.6}\text{S}_8$.

Given a constant iron to nickel atomic ratio of 4:1, the sample with lower metal concentration, $\text{Fe}_{6.15}\text{Ni}_{1.54}\text{S}_8$, showed a faster oxidation rate than its metal richer counterpart, $\text{Fe}_{6.4}\text{Ni}_{1.6}\text{S}_8$. The mean oxidation rates for these two samples are 1.85×10^{-4} and $1.22 \times 10^{-4} \text{ s}^{-1}$ respectively for 1.5 h heating at 830 K. Vyazovkin's theory of changing activation energy (E_a) with reaction extent (y) was employed in the current kinetic study. The activation energy was determined using a model-free method. The oxidation of $\text{Fe}_{6.4}\text{Ni}_{1.6}\text{S}_8$ exhibited a higher E_a than $\text{Fe}_{6.15}\text{Ni}_{1.54}\text{S}_8$ over the course of reaction. The activation energy increases with y from 67.1 to 103.3 kJ mol^{-1} for *mss* composition $\text{Fe}_{6.15}\text{Ni}_{1.54}\text{S}_8$; 76.1 to 195.0 kJ mol^{-1} for $\text{Fe}_{6.4}\text{Ni}_{1.6}\text{S}_8$.

Bulk compositions $\text{Fe}_{7.9}\text{S}_8$, $\text{Fe}_{2.37}\text{Ni}_{5.53}\text{S}_8$ were selected to give a constant metal to sulfur atomic ratio of 7.9:8. Oxidation of $\text{Fe}_{2.37}\text{Ni}_{5.53}\text{S}_8$ achieved equilibrium within 1 h, compared to 5 h for $\text{Fe}_{7.9}\text{S}_8$.

© 2004 Elsevier B.V. All rights reserved.

Keywords: Kinetics; Model free; Monosulfide solid solution; Oxidation; Phase evolution

1. Introduction

The monosulfide solid solution $(\text{Fe}, \text{Ni})_{1-x}\text{S}$, is an important precursor of primary iron–nickel sulfides in ore deposits. At high temperatures (>883 K) $(\text{Fe}, \text{Ni})_{1-x}\text{S}$ has the NiAs structure and is known as the monosulfide solid solution (*mss*). Above 883 K, there is complete solid solution

between Fe- and Ni-end-members; below this temperature it decomposes to form pyrrhotite and pentlandite [1]. The composition and stoichiometry of the monosulfide solid solution are variable but in nature it rarely exceeds Ni to Fe atomic ratio of 1:4. The variation in *mss* composition is due to the diversity of primary ore bodies as well as alterations due to supergene environment and weathering over geological time [2]. In this work, samples were prepared to give different iron to nickel atomic ratios (Fe:Ni) and different metal to sulfur ratios (M:S). The variable stoichiometry of *mss* leads

* Corresponding author. Tel.: +61 8 82077659; fax: +61 8 82077222.
E-mail address: haipeng.wang@adelaide.edu.au (H. Wang).

to different oxidation mechanisms as well as phase evolution procedures during the oxidation.

Violarite and pentlandite (often accompanied by pyrrhotite/*mss*) are important nickel ores used as feedstock in flash smelting processes to produce nickel matte [3]. Monosulfide solid solution is a common intermediate phase observed during the oxidation of violarite and pentlandite. Therefore, the investigation of *mss* oxidation is of benefit in understanding the thermal behavior of these economically important metal sulfides. In this work, oxidation temperature of 830 and 850 K were chosen, as they are above the onset decomposition temperature of these economic metal sulfides (violarite and pentlandite) to *mss*, 723 K [3,4].

Oxidation behaviors of economic metal sulfide ores under heating schedules have been well studied [3,5–7]. The oxidation of *mss* starts at a very low temperature under atmospheric conditions. The dominant oxidation products from *mss* are ferrous sulfate and hematite in the temperature range 413–483 K; ferrous sulfate starts decomposing to *mss* and hematite when the temperature reaches 733 K [5]. It was postulated by Sliullin and Gitis that *mss* is first converted to sulfate during oxidizing roasting before being converted to oxides [8]. Banerjee proposed that the oxidation of *mss* starts at relatively low temperatures where iron is preferentially oxidized to metal sulfate accompanied by the release of SO_2 [5]. At elevated temperatures, the iron (III) sulfate will be transformed to a porous Fe_2O_3 layer.

Oxidation studies on metal sulfides are generally carried out under three sets of conditions: (i) under hydrothermal conditions, (ii) under heating conditions, where the temperature increases at a steady rate, and (iii) under vigorously oxidizing conditions, where metal sulfides are ignited [2,9–13]. The thermodynamics and kinetics of metal sulfide oxidation were extensively investigated in each of these methods. However, these methods do not provide enough evidence to reveal the reaction mechanism and kinetic behavior under isothermal conditions. Metal sulfides oxidize in a stepwise reaction sequence with increasing temperature; different reactions in this sequence are governed by different reaction mechanisms. The reaction mechanisms can also be different for the same reaction, if undertaken at different temperatures. Kinetic studies under isothermal conditions, on the other hand, investigate the kinetic behavior during the oxidation at a constant temperature. The reaction mechanism can be better understood using isothermal kinetic data and phase evolution evidence acquired from isothermal experiment. This work focused on the oxidation behaviors of *mss* under isothermal conditions.

The oxidation rate of *mss* is also dependent on particle size and oxygen partial pressure. Smaller particle size and increased oxygen partial pressure accelerate the process of oxidation. However, when the temperature exceeds 825 K the particle size effect becomes less significant and the oxidation rate is virtually independent of the particle size [7]. The applicability of this result to the current study remains uncertain but carrying out the oxidation experiment at ele-

vated temperatures certainly will reduce the affect of particle size on the oxidation rate. To simplify the kinetic analysis, the current oxidation study was performed in an air atmosphere at 830 and 850 K. The particle size was confined to the range 53–90 μm . The experimental kinetic results only apply to this specified particle range. The effect of particle size on the oxidation kinetics is not concerned in this paper.

Earlier works on oxidation and thermal decomposition of metal sulfides concentrated on natural samples from various ore deposits, which contained different types of impurities [5,8]. The present study is confined to synthetic samples, which minimize the complexity of analysis caused by trace impurities in natural sulfides. Generalized mechanisms derived from experiments on synthetic samples may also apply to natural samples.

2. Experimental

2.1. Synthesis

The standard silica-tube techniques [1,14] were adopted to synthesize the monosulfide solid solution (*mss*). Accurately weighed stoichiometric amounts of Fe (1 mm diameter wire, 99.9+%, Aldrich), Ni (1 mm diameter wire 99.9+%, Aldrich) and S (granules 99.99+%, Aldrich) were sealed under vacuum in 10 mm diameter silica tubes. Bulk compositions of *mss* $\text{Fe}_{7.9}\text{S}_8$, $\text{Fe}_{2.37}\text{Ni}_{5.53}\text{S}_8$, $\text{Fe}_{6.15}\text{Ni}_{1.54}\text{S}_8$, $\text{Fe}_{6.4}\text{Ni}_{1.6}\text{S}_8$ were selected to provide different iron and nickel contents as well as different metal to sulfur ratios. The charges were heated slowly to 573 K, then up to 773 K and finally to 1073 K, soaking for 12 h at each stage [15,16]. The slow heating schedule and soaking process were employed to minimize tube failure due to the high sulfur vapour pressure above 723 K. The tubes were quenched to room temperature in cold water. The charges were removed from the tubes and ground to fine powder under acetone, ensuring the homogeneity of the *mss*. The charges were then resealed in silica tubes and heated at 1373 K for 2 h, cooled to 1173 K, annealed for 7 days, and then quenched in a large volume of cold water. This resulted in homogenous samples with a relatively uniform 0.5 mm grain size.

2.2. Oxidation

Mss samples were ground to fine power using an agate mortar and then sieved to ensure particle size ranging from 53 to 90 μm . Each charge of 0.1 g *mss* powder was placed in an open platinum crucible. Oxidation experiments were performed in a muffle furnace (Kilnwest Ltd.) at 830 and 850 K, 1 atm. The samples were placed in the preheated furnace and a series of oxidation periods ranging from 0.5 to 24 h were adopted. The platinum crucibles containing the oxidized samples were carefully removed from the furnace with a pair of tweezers and then quenched by only dipping the

bottom of the crucible into water, avoiding water contamination. The temperatures were controlled within an error range ± 5 K.

2.3. X-ray diffraction

Room temperature X-ray diffraction patterns of the quenched products were obtained using a *Guinier Hagg* camera with Cr $K\alpha_1$ radiation ($\lambda = 2.2897 \text{ \AA}$). Samples were ground with acetone in an agate mortar and pestle to produce an optimum grain size below $10 \mu\text{m}$. The finely powdered sample was mixed with a small amount of pure Si, which acted as an internal standard. The *Guinier Hagg* films were scanned in *TPU/Pos* mode using an Epson film scanner and the powder diffraction profile over 2θ range $10\text{--}90^\circ$ was extracted using the program *Scion Image* and the *Universal-Si-Calibration*, a macro function based on *Igor Pro* Version 4.0 [17].

The *Rietveld* method [18,19] was used to analyse the X-ray powder diffraction profiles. This method reveals the detailed structure and composition of a polycrystalline sample [20]. The *Pseudo-Voigt* function was adopted to model the peak shapes of X-ray diffraction patterns. Refined parameters were: peak shape variables (U, V, W), background (*Shifted Cheby* I function), scale factor (S), cell parameters ($a, b, c, \alpha, \beta, \gamma$), and thermal displacement (B). The refinement of these parameters integrates each intensity into a properly shaped reflection, which contributes to the overall diffraction pattern. The result is a calculated X-ray diffraction profile, which best-fits the experimental intensities of X-ray diffraction peak. GOF (goodness of fit) was used to assess the success or otherwise of the refinement procedure.

Quantitative phase analysis was performed on oxidized samples using the formalism described by Hill and Howard [21]. The general scattering cross-section for *Bragg* scattering (scale factor S) is proportional to N/V , where N is the number of unit cells contributing to the scattering and V the unit cell volume [22]. The weight fraction of a phase can be described as:

$$w_i = \frac{(SZMV)_i}{\sum (SZMV)_i} \quad (1)$$

where w_i is the weight fraction of phase i , S the scale factor, Z the number of formula units per unit cell, M the molecular weight of the formula unit, and V the volume of unit cell.

Any variation of the stoichiometry of *mss* over the course of oxidation will be reflected in changes in the cell parameters. Thus, the cell parameters are refined for each X-ray powder profile. Initial input cell parameters and atom positions for the *Rietveld* refinement were taken from Alsen for $(\text{Fe}, \text{Ni})_{1-x}\text{S}$, Collin et al. for $\text{Ni}_{17}\text{S}_{18}$, Pearson and Buerger for $(\text{Fe}_{4.5}\text{Ni}_{4.5})\text{S}_9$, Pauling and Hendricks for Fe_2O_3 , and Christidis and Rentzeperis for $\text{Fe}_2(\text{SO}_4)_3$ [23–27].

2.4. SEM examination

Samples of three different bulk compositions of *mss* series, $\text{Fe}_{7.9}\text{S}_8$, $\text{Fe}_{2.37}\text{Ni}_{5.53}\text{S}_8$, $\text{Fe}_{6.15}\text{Ni}_{1.54}\text{S}_8$ were examined using a PHILIPS XL20 scanning electron microscope to reveal surface feature evolution during oxidation. Non-oxidized *mss* specimens were polished to produce smooth surfaces, and then placed in a preheated muffle furnace oxidized for up to 24 h at 830 K (dry air atmosphere).

3. Kinetic theory

Solid-state reaction kinetics is based on the *Activated State* theory, where the reaction rate can be written as:

$$\frac{dy}{dt} = kf(y) \quad (2)$$

where y is the reaction extent, k the rate constant, and $f(y)$ the function of kinetic model.

Under current experimental conditions, the results show that the Fe in *mss* was oxidized to hematite, whilst Ni was eventually transformed to $\text{Ni}_{17}\text{S}_{18}$, a phase which has the pyrrhotite structure. Either hematite or $\text{Ni}_{17}\text{S}_{18}$ (wt.%) can be used to determine the extent of reaction. As most of the *mss* compositions examined were Fe-rich, the reaction extent was calculated on the basis of hematite fraction to minimize systematic errors amplified by mathematical calculation. The weight percentage of hematite was converted into reaction extent (y) using the following equation:

$$y = \frac{w_t - w_0}{w_e - w_0} \times 100\% = \frac{w_t}{w_e} \times 100\% \quad (w_0 = 0) \quad (3)$$

where y is the reaction extent; w_0, w_e, w_t are the weight fractions of hematite, at the beginning of reaction ($t = 0$), at the end of reaction ($t = \infty$) and at an arbitrary time t , respectively [16,28]. Assuming complete oxidation of Fe to hematite, the calculated equilibrium weight fraction of hematite was derived by mass balance. The kinetic behavior of *mss* oxidation can be investigated by inspecting the relationship between reaction extent (y) and reaction time (t).

It is well known that rate constants are exponentially dependent on the inverse of absolute temperature. The dependence of k on temperature has the general form of the *Arrhenius* equation:

$$k = A \exp\left(\frac{E_a}{RT}\right) \quad (4)$$

The disadvantage of this method is that the calculated value of k depends on the empirical selection of the function $f(y)$, the kinetic model in Eq. (2) and therefore E_a depends on the choice of rate equation. Unfortunately, a number of different forms of the rate equation may fit the data equally well, but result in different values of E_a [29].

A second disadvantage is that it assumes that E_a does not change during the course of an isothermal transformation.

Vyazovkin explained the dependence of activation energy on reaction extent, caused by changing physical and mechanical properties of reaction medium [30].

Vyazovkin discussed isoconversional methods that employ the notion of the dependence of the activation energy on the reaction extent to predict the kinetic behavior of a reaction outside of the range of experimental temperatures [31]. Model-free methods can be adopted to avoid the problems associated with choosing an over simplified kinetic model. Vyazovkin and Dollimore introduced a unified approach to kinetic processing of non-isothermal data [32].

In this work, isothermal data were used to calculate E_a . It is postulated that E_a is a function of y . Hence, the basic kinetic equation can be rewritten as:

$$\frac{dy}{dt} = k(T, y)f(y) \quad (5)$$

where T is the absolute temperature, $k(T, y)$ the rate constant and $f(y)$ of a kinetic model. Rewriting Eq. (5) and substituting Eq. (4) for $k(T, y)$ give,

$$\ln \frac{dy}{dt} = \ln A + \ln f(y) - \frac{E_a(y)}{RT}$$

For a given segment of the reaction $y = y_0$, $\ln f(y_0)$ and $E_a(y_0)$ are constant. Therefore, the model-free determination of E_a gives:

$$E_a(y_0) = -R \frac{\ln dy/dt(y_0, T_1) - \ln dy/dt(y_0, T_2)}{(1/T_1 - 1/T_2)} \quad (6)$$

where $dy/dt(y_0, T_1)$ and $dy/dt(y_0, T_2)$ are reaction rates to a given value of y_0 at two different temperatures T_1 and T_2 , respectively.

4. Results and discussion

4.1. Oxidation mechanism

Although the oxidation mechanism of metal sulfides has been addressed by a number of researchers, general conclusions have not been established [5–7]. A popular hypothesis, the “Shrinking-Unreacted Core” model is widely accepted [33,34]. According to this theory, solid particles in an oxygen gas stream are oxidized through gaseous diffusion of O_2 to the reaction interfaces and controlled by the rates of both chemical reaction and mass transport [4]. The *mss* oxidation is initiated at the grain surfaces and then moves towards the unreacted shrinking core. Chamberlain states that, for the oxidation of *mss*, the particles pass through an induction stage, during which sulfur is disassociated from the surface and gaseous sulfur oxides are released [4]. The kinetic data from the current study show that the oxidation of *mss* is so rapid that the induction stage could not be identified due to the difficulty of collecting data on a very short time frame. The experimental data indicate that the *mss* oxidation is a simple decelerating process. It starts at a rela-

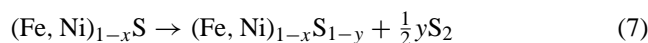
tive high reaction rate and levels out at the end, due to the thickening of the inhibiting oxide layer. The ever-thickening oxide layer results in a porous surface [35–39]. The porosity of the oxide layer is caused by sulfur evolution during the induction stage of oxidation [2]. Fig. 1 shows the porous surfaces of samples: $Fe_{7.9}S_8$, $Fe_{6.15}Ni_{1.54}S_8$, $Fe_{2.37}Ni_{5.53}S_8$, after being oxidized at 830 K for 1, 1 and 1.5 h, respectively. The EDX composition analysis shows a slightly lower sulfur and higher oxygen content around the pits than that of the smooth surfaces (in Fig. 1). However, no statistically valuable data were obtained due to the small size and high concentration of the pits. Most of the EDX data were more like average compositions of the void and smooth surface. For the composition $Fe_{7.9}S$, EDX shows that after prolonged oxidation virtually no sulfur was detected on the granular surface. Similarly, a distinct decrease in sulfur content occurred for the oxidation of other *mss* compositions. These results indicate the continuous release of sulfur during the oxidation of *mss*.

X-ray diffraction profiles of the oxidized *mss* samples demonstrate that the Fe is preferentially oxidized to hematite; Ni, instead, is finally transformed to $Ni_{17}S_{18}$. This conforms to the results of previous researchers [40–46]. Dunn [47] and Chamberlain and Dunn [48] proposed that during the oxidation of metal sulfides, Fe migrates towards the outer rim where it is preferentially oxidized leaving a Ni-rich *mss* core. This preferential oxidation occurs once the partial pressure of the evolved sulfur gas decreases sufficiently to allow the diffusion of oxygen through the porous layer.

For the Ni free sample $Fe_{7.9}S_8$, the oxidation of Fe (within the first hour of reaction) leaves a much more distinctly porous surface than that of the sample $Fe_{6.15}Ni_{1.54}S_8$ (Fig. 1a–d). These micrographs of Fe-rich and pure Fe *mss* samples show the evolving surface features, from porous to grainy, during oxidation. For the Ni-rich sample $Fe_{2.37}Ni_{5.53}S_8$, a surface with sporadic pits does not appear until the oxidation reaches equilibrium (Fig. 1e and f).

4.2. Oxidation reactions

Oxidation products of *mss* were determined from the powder X-ray diffraction profiles. The intermediate and final products of the oxidation are dependent on the stoichiometry of *mss*. The desulfuration and release of SO_2 are responsible for the induction stage of the oxidation [4]. The major reactions at this stage are:



Following the induction stage, the principal reaction is the preferential oxidation of iron in *mss* to hematite. The onset temperature of this reaction remains unsolved, although a wide range of temperatures have been reported for this reaction [4–8]. In the current study,

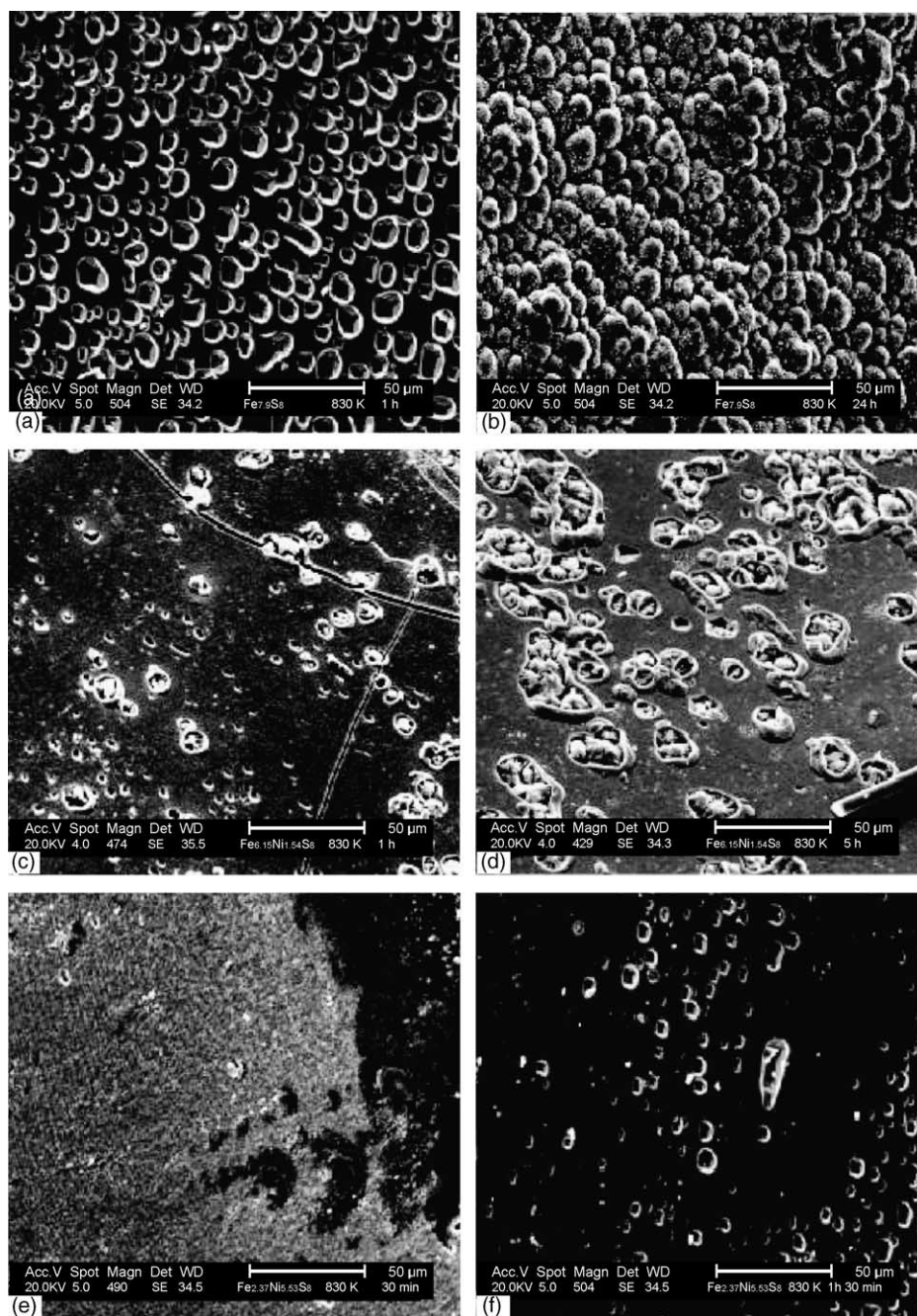


Fig. 1. SEM micrographs of the surface feature for oxidized *mss* samples. The oxidation was performed at 830 K, 1 atm. Micrographs (a) and (b) were taken after 1 and 24 h oxidation for $\text{Fe}_{7.9}\text{S}_8$; (c) and (d): 1 and 5 h oxidation for $\text{Fe}_{6.15}\text{Ni}_{1.54}\text{S}_8$; (e) and (f): 0.5 and 1.5 h oxidation for $\text{Fe}_{2.37}\text{Ni}_{5.53}\text{S}_8$.

hematite was observed as the major oxidation product of *mss* at 830 and 850 K. Some minor or intermediate phases were also identified in the X-ray powder diffraction profiles.

For the pure Fe *mss* ($\text{Fe}_{7.9}\text{S}_8$), hematite, mikasaite ($\text{Fe}_2(\text{SO}_4)_3$) and residual *mss* were identified in the charge after 24 h oxidation at 830 K in air (Table 1). For Fe–Ni *mss* compositions, hematite and $\text{Ni}_{17}\text{S}_{18}$ were observed as the final oxidation products for experiments carried out under the same conditions. Magnetite was not observed, which

contradicts the results of Asaki et al. [6]. Magnetite, if present, is below the detection limits of *Rietveld* profile fitting methods (around 1 wt.% of product). Apart from these main oxidation products, up to 5.7 wt.% of an intermediate phase, pentlandite, was observed for the sample $\text{Fe}_{6.4}\text{Ni}_{1.6}\text{S}_8$ (Tables 2 and 3). Pentlandite was not an equilibrium product in this oxidation. Exsolved pentlandite was eventually oxidized to produce hematite and $\text{Ni}_{17}\text{S}_{18}$. Pentlandite will exsolve from *mss* when *mss* is heated above 450 K [15]. It was reported that the activation energy of pentlandite exsolution

Table 1
Phase evolution during the oxidation of nickel-free *mss* (Fe_{7.9}S₈) at 830 K

Time (h)	wt.% mik.	<i>a</i> _{mik} (Å)	<i>c</i> _{mik} (Å)	wt.% <i>mss</i>	<i>a</i> _{<i>mss</i>} (Å)	<i>c</i> _{<i>mss</i>} (Å)	<i>V</i> _{<i>mss</i>} (Å ³)	wt.% hem.	<i>a</i> _{hem} (Å)	<i>c</i> _{hem} (Å)
0.0				99.9(2)	3.4506(2)	5.8156(6)	59.968(7)			
1.0	1.1(2)	8.236(1)	22.178(3)	72.3(8)	3.4479(3)	5.7314(9)	59.01(1)	26.6(6)	5.026(2)	13.764(5)
5.0	5.7(2)	8.235(1)	22.177(3)	15.3(6)	3.4488(7)	5.5443(2)	57.09(3)	79.0(8)	5.0234(6)	13.781(2)
24.0	5.4(2)	9.237(1)	22.176(3)	14.5(6)	3.4486(7)	5.5422(2)	57.08(3)	80.1(8)	5.0238(5)	13.775(2)

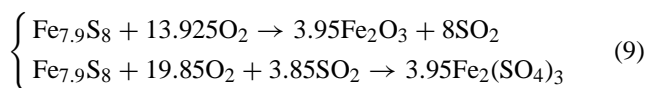
Summary of cell parameters and unit cell volume for each phase: wt.% mik., wt.% *mss*, wt.% hem. are weight fractions for mikasaite, *mss* and hematite. *a*_{mik}, *c*_{mik} are cell parameters for mikasaite; *a*_{*mss*}, *c*_{*mss*} and *V*_{*mss*} for *mss*; *a*_{hem}, *c*_{hem} for hematite. Estimated standard deviations are given in brackets.

Table 2
Phase evolution during the oxidation of iron–nickel *mss* at 830 K

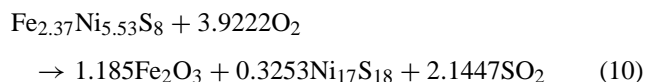
Initial bulk composition	Time (h)	wt.% pent.	<i>a</i> _{pent} (Å)	<i>V</i> _{pent} (Å ³)	wt.% <i>mss</i>	<i>a</i> _{<i>mss</i>} (Å)	<i>c</i> _{<i>mss</i>} (Å)	<i>V</i> _{<i>mss</i>} (Å ³)	wt.% hem.	<i>a</i> _{hem} (Å)	<i>c</i> _{hem} (Å)
Fe _{6.4} Ni _{1.6} S ₈	0.0				100.0(4)	3.4501(6)	5.810(1)	59.89(2)			
	0.5	1.5(7)	10.105(3)	1032.0(6)	80.3(8)	3.4521(1)	5.7546(5)	59.390(6)	18.2(7)	5.025(1)	13.767(4)
	1.0	5.7(7)	10.110(3)	1033.2(5)	53.9(7)	3.4505(6)	5.496(1)	56.67(2)	40.4(8)	5.041(2)	13.783(5)
	1.5	1.8(7)	10.118(5)	1035.8(6)	45.8(8)	3.4496(5)	5.416(1)	55.81(2)	52.4(7)	5.024(1)	13.787(3)
	5.0				23.1(7)	10.258(2)	15.991(6)	1457.4(8)	76.9(8)	5.0304(5)	13.756(2)
	24.0				23.2(7)	10.259(3)	16.008(7)	1459.1(9)	76.8(8)	5.031(1)	13.759(3)
Fe _{6.15} Ni _{1.54} S ₈	0.0				99.9(3)	3.4477(6)	5.772(1)	59.42(2)			
	0.5				64.5(6)	3.4488(5)	5.542(1)	57.09(2)	35.5(8)	5.018(1)	13.778(4)
	1.0				36.1(8)	3.4481(5)	5.402(1)	55.63(2)	63.9(8)	5.0218(9)	13.768(3)
	1.5				24.1(8)	10.251(3)	16.018(7)	1457.7(9)	75.9(6)	5.031(1)	13.759(3)
	5.0				23.6(8)	10.251(3)	16.020(6)	1457.9(8)	76.4(7)	5.030(1)	13.754(3)
Fe _{2.37} Ni _{5.53} S ₈	0.0				99.9(2)	3.4489(6)	5.530(1)	56.96(2)			
	0.5				77.7(7)	3.4418(8)	5.384(1)	55.23(2)	22.3(7)	5.013(2)	13.735(7)
	1.0				73.3(6)	10.368(1)	15.959(4)	1485.6(4)	26.7(4)	5.035(1)	13.772(6)
	1.5				74.2(8)	10.367(1)	15.960(3)	1485.4(4)	25.8(4)	5.035(2)	13.786(6)

Summary of cell parameters and unit cell volume for each phase: wt.% pent., wt.% *mss*, wt.% hem. are weight fractions for pentlandite, *mss* and hematite. *a*_{pent}, *V*_{pent} are cell parameters for pentlandite; *a*_{*mss*}, *c*_{*mss*} and *V*_{*mss*} for *mss*; *a*_{hem}, *c*_{hem} for hematite. Estimated standard deviations are given in brackets.

from *mss* is very low (around 5 kJ mol⁻¹) at the beginning of the exsolution for *mss* composition Fe_{6.4}Ni_{1.6}S₈ [15]. This may explain the observation of pentlandite during the oxidation of Fe_{6.4}Ni_{1.6}S₈. The proposed oxidation reactions for these *mss* samples are: For Fe_{7.9}S₈,



For Fe_{2.37}Ni_{5.53}S₈,



For Fe_{6.15}Ni_{1.54}S₈,

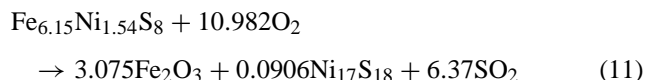


Table 3
Phase evolution during the oxidation of iron–nickel *mss* at 850 K

Initial bulk composition	Time (h)	wt.% pent.	<i>a</i> _{pent} (Å)	<i>V</i> _{pent} (Å ³)	wt.% <i>mss</i>	<i>a</i> _{<i>mss</i>} (Å)	<i>c</i> _{<i>mss</i>} (Å)	<i>V</i> _{<i>mss</i>} (Å ³)	wt.% hem.	<i>a</i> _{hem} (Å)	<i>c</i> _{hem} (Å)
Fe _{6.4} Ni _{1.6} S ₈	0.0				100.0(3)	3.4499(5)	5.809(2)	59.87(2)			
	0.5	0.9(7)	10.105(3)	1031.8(5)	70.6(6)	3.4501(4)	5.662(1)	58.37(2)	28.5(7)	5.024(1)	13.777(4)
	1.0	5.1(7)	10.108(3)	1032.8(5)	41.8(6)	3.4509(5)	5.401(1)	55.70(2)	53.1(7)	5.026(2)	13.779(3)
	2.0				27.7(6)	3.4506(5)	5.346(1)	55.13(2)	72.3(7)	5.024(1)	13.783(3)
	3.0				23.2(6)	10.256(2)	16.011(6)	1458.5(8)	76.8(7)	5.029(2)	13.765(3)
	5.0				23.0(6)	10.259(2)	16.008(7)	1459.1(8)	77.0(7)	5.030(1)	13.768(3)
Fe _{6.15} Ni _{1.54} S ₈	0.0				100.0(3)	3.4478(5)	5.770(2)	59.40(2)			
	0.5				49.4(7)	3.4485(5)	5.448(1)	56.11(2)	50.6(8)	5.020(1)	13.774(3)
	0.75				32.5(7)	3.4481(5)	5.398(2)	55.58(2)	67.5(8)	5.024(1)	13.770(3)
	1.0				24.9(7)	10.254(3)	16.022(5)	1458.9(8)	75.1(7)	5.032(1)	13.761(3)
	1.5				23.3(6)	10.255(3)	16.021(6)	1459.1(8)	76.7(7)	5.032(1)	13.757(3)
	2.0				23.4(6)	10.254(3)	16.023(6)	1459.0(8)	76.6(7)	5.030(1)	13.758(3)

Summary of cell parameters and unit cell volume for each phase: wt.% pent., wt.% *mss*, wt.% hem. are weight fractions for pentlandite, *mss* and hematite. *a*_{pent}, *V*_{pent} are cell parameters for pentlandite; *a*_{*mss*}, *c*_{*mss*} and *V*_{*mss*} for *mss*; *a*_{hem}, *c*_{hem} for hematite. Estimated standard deviations are given in brackets.

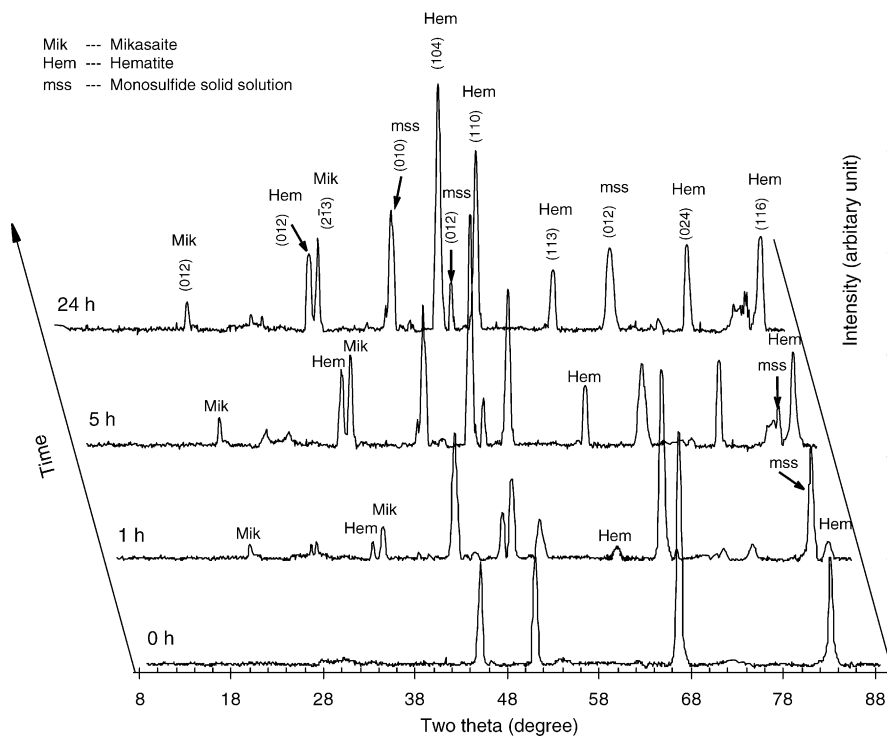
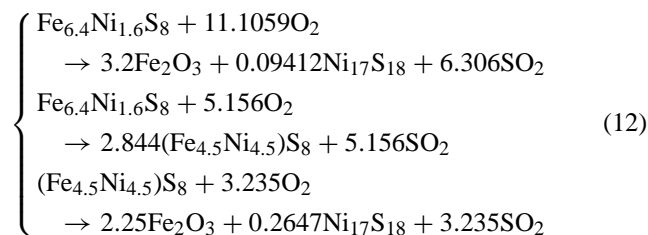


Fig. 2. Stack of X-ray powder diffraction patterns showing the progress of phase evolution during the oxidation of $Fe_{7.9}S_8$. The oxidation was taken under isothermal condition (830 K, 1 atm.). The time range for oxidation varied from 0 to 24 h.

For $Fe_{6.4}Ni_{1.6}S_8$,



4.3. Phase evolution

The pure iron *mss* $Fe_{7.9}S_8$ samples were oxidized at 830 K in air for periods up to 24 h. Fig. 2 shows the phases evolution over the oxidation. Diffraction patterns were collection at 0, 1, 5 and 24 h. The major oxidation product was hematite. A minor phase, mikasaite ($Fe_2(SO_4)_3$), was also detected. Distinct mikasaite peaks (0 1 2) and (2 $\bar{1}$ 3) were observed after 1 h. The diffraction intensity of mikasaite (iron (III) sulfate) increased to a maximum after 5 h and remained unchanged till the end of the oxidation experiment. The *Rietveld* resolved phase fraction of iron (III) sulfate increased up to 5.7 wt.% then remained constant after prolonged oxidation of pure Fe *mss* at 830 K. Following this stage, the oxidation is retarded and the oxide layer growth follows a parabolic rate law, where mass transfer through the gaseous boundary layer at sample surface and diffusion of oxygen through the oxide layer control the progress of oxidation. Banerjee detected iron (II) and (III) sulfates during the oxidation experiment of pyrrhotite.

The iron (II) sulfate is more likely a precursor of iron (III) sulfate. In the current study iron (II) sulfate is not detected by XRD. This may due to the fast conversion rate of iron (II) to iron (III) at elevated temperatures, and the lack of data collected in very short time frames at the beginning of the reactions [5].

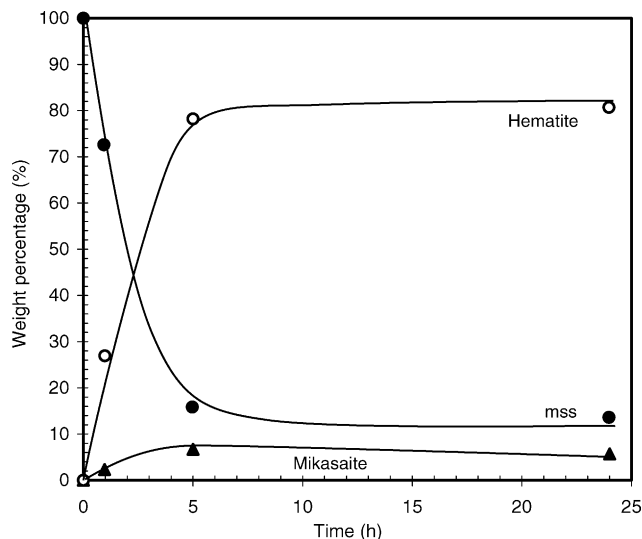


Fig. 3. Plot showing the progress of iron oxidation to hematite, producing mikasaite and decreasing weight fraction of *mss* during the oxidation of $Fe_{7.9}S_8$ at 830 K, 1 atm. The circle symbol represents the weight fraction of hematite; solid circle, for *mss*; solid triangle, for mikasaite. The curves are produced using least-square method to best-fit experimental data.

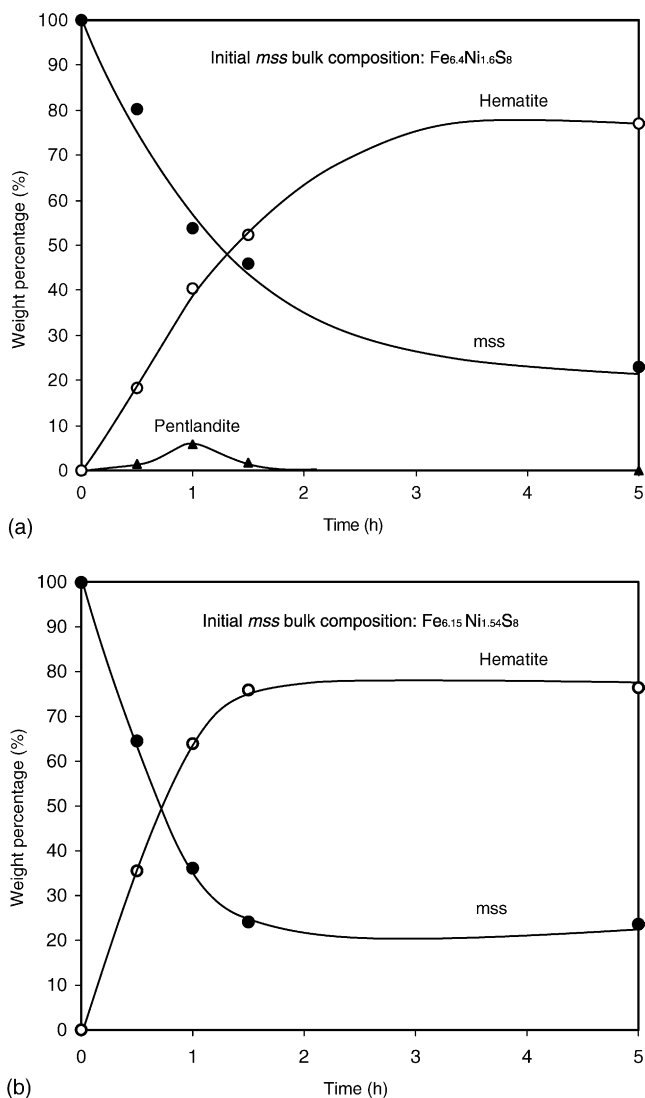


Fig. 4. Plot showing the evolving phase fractions during the oxidation of *mss* samples Fe_{6.4}Ni_{1.6}S₈ (a) and Fe_{6.15}Ni_{1.54}S₈ (b) at 830 K, 1 atm. Symbols (○), (●) and (▲) are the representative for the weight percentage of hematite, *mss*, and pentlandite, respectively.

The weight fractions of each phase versus oxidation time are shown in Fig. 3. It is clear that the reaction rate was very rapid at the beginning and levelled out after 5 h annealing. It is worth noting that the residual *mss* was not oxidized even after prolonged oxidation. It was also observed that the former finely powdered samples formed hard conglomerates during oxidation. This inhibited the diffusion of oxygen and left an unreacted *mss* core.

The phase evolutions for the nickel containing (iron rich) *mss* samples, Fe_{6.4}Ni_{1.6}S₈ and Fe_{6.15}Ni_{1.54}S₈ are shown in Fig. 4a and b. The compositions of both samples were chosen to give an Fe:Ni atomic ratio of 4:1 but with different metal to sulfur ratios, 0.96:1 and 1:1, respectively. Hematite and Ni₁₇S₁₈ are the major final products (also see Eqs. (11) and (12)). An intermediate phase, pentlandite, was observed for the composition richer in metal Fe_{6.4}Ni_{1.6}S₈. The phase

fraction of pentlandite reached a maximum after oxidation for 1 h. The following continuous decrease of pentlandite can be explained by the oxidation of pentlandite. Different onset decomposition temperatures of pentlandite have been reported by several researchers [2,4]. The maximum onset decomposition temperature of pentlandite was reported at 883 K, where Fe to Ni ratio was 1:1 [49]. This temperature decreased rapidly as the Fe to Ni atomic ratio deviated from the ideal value of 1:1. In the current oxidation study, the intermediate phase, pentlandite (exsolved from *mss*), is believed to have a changing Fe:Ni ratio. This may explain the lower oxidation temperature for pentlandite in this work. The composition of pentlandite can be determined from its cell edge [15]. Using the cell parameter data in Table 2, the calculated pentlandite compositions are Fe_{4.5}Ni_{4.5}S₈, Fe_{4.9}Ni_{4.1}S₈, and Fe_{5.6}Ni_{3.4}S₈ after *mss* Fe_{6.4}Ni_{1.6}S₈ was oxidized at 830 K for 0.5, 1.0 and 1.5 h, respectively.

The exsolution of pentlandite from the host phase and its subsequent oxidation are competitive steps, which result in a maximum weight fraction of pentlandite at some time during oxidation. Increasing metal content retards the oxidation of the metal sulfide but facilitates the pentlandite exsolution from the *mss* host [15,48,50]. In the current study, pentlandite was only observed in the metal richer sample (Fe_{6.4}Ni_{1.6}S₈), which is related to the rapid exsolution of pentlandite from *mss* at the beginning of reaction. For the more sulfur rich sample (Fe_{6.15}Ni_{1.54}S₈), the accelerated oxidation rate overwhelmed the decelerated exsolution rate of pentlandite and no pentlandite was detected.

The oxidation of the Ni-rich sample, Fe_{2.37}Ni_{5.53}S₈ (830 K, 1 atm.) reached equilibrium within 1 h and yielded 26.7 wt.% hematite and 74.2 wt.% Ni₁₇S₁₈.

4.4. Structural modification

It is shown in Tables 1–3 that the cell parameters for hematite and mikasaite did not change significantly, when ex-

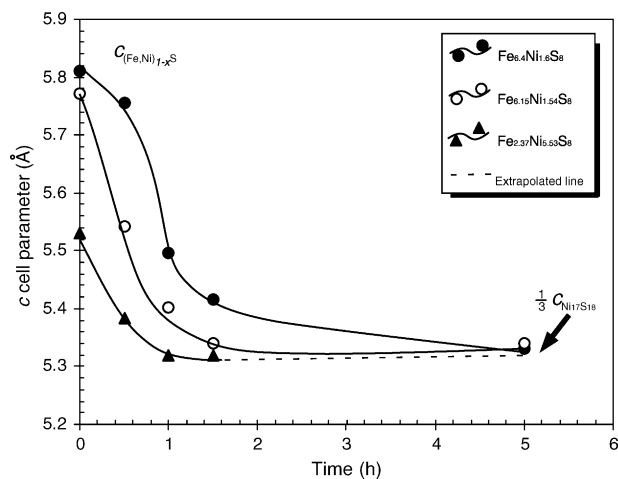


Fig. 5. Plot of *c* parameter versus retaining time over the oxidation at 830 K for three iron–nickel *mss* compositions (Fe_{6.4}Ni_{1.6}S₈, Fe_{6.15}Ni_{1.54}S₈ and Fe_{2.37}Ni_{5.53}S₈).

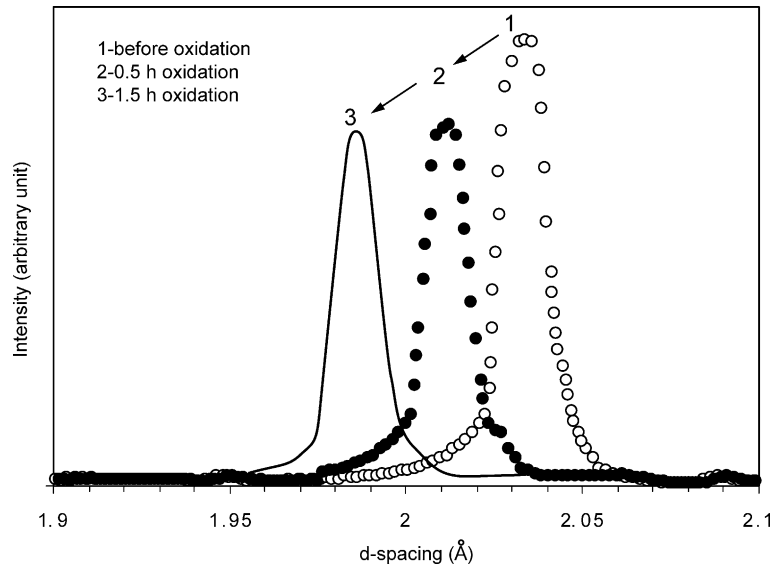


Fig. 6. Plot showing the shift of (012) peak in the X-ray profile of *mss* ($\text{Fe}_{2.37}\text{Ni}_{5.53}\text{S}_8$) during the oxidation at 830 K. The symbol (\circ), (\bullet) and solid curve represent the X-ray intensity for samples prior to oxidation, after 0.5 and 1.5 h oxidation.

perimental uncertainties are considered, during the oxidation indicating their compositions remains more or less constant on the time scale of these experiments. For *mss*, on the other hand, some distinct variation in the cell parameters was observed over the course of oxidation. This was caused by the

variation of stoichiometry of *mss*. In general, sulfur-rich *mss* produces more cation vacancies, which results in a smaller unit cell volume. Replacing Fe with Ni also reduces unit cell volume of *mss*, especially the *c* parameter due to the smaller atomic diameter of Ni [51]. Fig. 5 shows the variation of the *c*

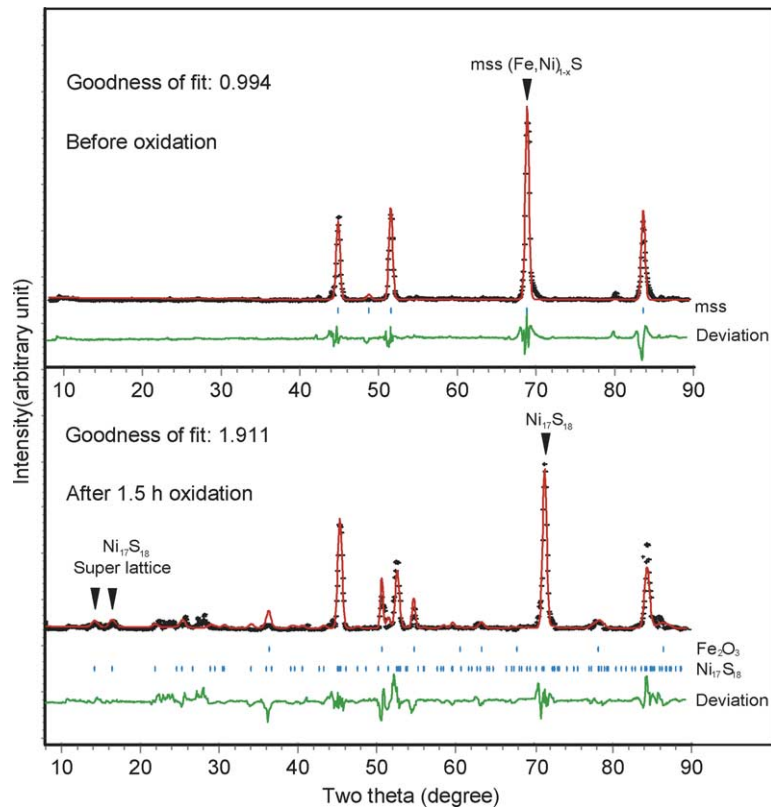


Fig. 7. The X-ray diffraction patterns taken before and after oxidation at 830 K for *mss* sample $\text{Fe}_{2.37}\text{Ni}_{5.53}\text{S}_8$. The appearance of two distinct diffraction peaks at small $2\theta = 14.1^\circ$ and 16.1° (d -spacing = 8.9396 and 7.8024 Å) indicated the formation of super-lattice for *mss*.

parameter for three iron–nickel *mss* samples ($\text{Fe}_{2.37}\text{Ni}_{5.53}\text{S}_8$, $\text{Fe}_{6.15}\text{Ni}_{1.54}\text{S}_8$, $\text{Fe}_{6.4}\text{Ni}_{1.6}\text{S}_8$) during the oxidation at 830 K. The c parameters for these samples start from 5.530, 5.772 and 5.810 Å respectively at the beginning of oxidation. The smallest c parameter of *mss* corresponds to the most nickel-rich sample, and the largest for the most Fe and also metal rich sample. As the oxidation progressed, the c parameter for all the three samples converged to a value around 5.330 Å. This is related to the formation of $\text{Ni}_{17}\text{S}_{18}$. The preferential oxidation of Fe in *mss* to hematite left a progressively nickel-enriched *mss* and eventually an almost pure nickel compound, $\text{Ni}_{17}\text{S}_{18}$ (pyrrhotite-type structure), at the end of oxidation. The ever nickel-enriching *mss* results in a decreasing c parameter during the oxidation. This is characterized by the (0 1 2) peak shifting to a smaller d -spacing in the X-ray diffraction pattern of *mss*. Fig. 6 shows that the (0 1 2) peak moved from d -spacing 2.0336 to 1.9858 Å after 1.5 h oxidation at 830 K for the *mss* composition $\text{Fe}_{2.37}\text{Ni}_{5.53}\text{S}_8$.

X-ray patterns were collected for these samples after the oxidation reaction reached equilibrium. The occurrence of two distinct diffraction peaks at d -spacing = 7.8024 and 8.9396 Å (correspond to the planes (0 1 0) and (0 1 1) of nickel sulfide $\text{Ni}_{17}\text{S}_{18}$) after the oxidation of sample $\text{Fe}_{2.37}\text{Ni}_{5.53}\text{S}_8$ for 1.5 h, indicates the formation of a super-lattice of $\text{Ni}_{17}\text{S}_{18}$ (Fig. 7). These peaks conformed to the X-ray diffraction profile of the $\text{Ni}_{17}\text{S}_{18}$ with space group $P32$, which was reported by Collin et al. [24]. It appears that the *mss* evolved from an iron–nickel *mss* with space group $P6/mmc$ at the beginning of oxidation to a pure nickel sulfide ($\text{Ni}_{17}\text{S}_{18}$) with space group $P32$ at the end. The super-lattice of $\text{Ni}_{17}\text{S}_{18}$ has a tripled c parameter compared to the hexagonal iron–nickel *mss* (Fig. 8). The cell projections along [0 1 0] for (Fe, Ni)S and $\text{Ni}_{17}\text{S}_{18}$ show that the structural modification of *mss* from space group $P6/mmc$ to $P32$ is a topotactic transition in which the anionic array is unchanged during the transition but cation is replaced and reorganization occurs, as $(\text{Fe, Ni})_{1-x}\text{S} \rightarrow \text{Ni}_{17}\text{S}_{18}$.

4.5. Oxidation kinetics

The oxidation of *mss* has multi steps, involving various reactions. These make its kinetic analysis difficult, as the mechanisms cannot be elucidated in detail for every step. For mineral reactions of this type, the true functional form of the reaction model is almost never known, thus the Vyazovkin's notion of model-free determination of E_a should be applied to the kinetic study of *mss* oxidation in order to avoid any over simplified assumption of the kinetic models. The calculated E_a is empirical activation energy for the overall oxidation process, and is not confined to a specific step. The E_a varies with the reaction extent (y).

The effect of stoichiometry on the kinetic behavior of *mss* oxidation was investigated. Reaction extent was determined using Eq. (3). We assumed that all Fe in *mss* was oxidized to hematite and the Ni transformed to $\text{Ni}_{17}\text{S}_{18}$ at the end of oxidation. This hypothesis was verified by comparing the calculated and measured hematite weight fraction after oxidation

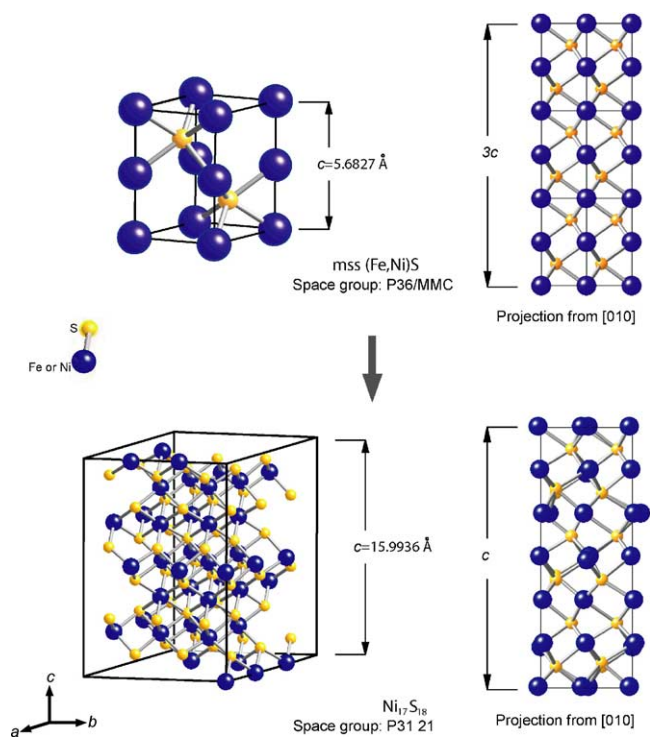


Fig. 8. Comparison of the crystal structure between iron–nickel *mss* (Fe, Ni)S and the nickel sulfide $\text{Ni}_{17}\text{S}_{18}$. The (Fe, Ni)S unit cell is enlarged for the purpose of good illustration.

achieved equilibrium (Table 4). The theoretical equilibrium hematite weight fractions are in good agreement with our experimental results, except for the *mss* composition $\text{Fe}_{7.9}\text{S}_8$. This may be caused by the effect of sintering of the finely grinded *mss* ($\text{Fe}_{7.9}\text{S}_8$) powder during the oxidation.

The samples were placed in a reheated furnace. If the samples were ignited at the elevated temperature, the surface temperature of these samples will differ from that of the furnace, and the calculated activation energies would have no general thermodynamic meaning. The possible ignited *mss* composition under current experimental conditions is $\text{Fe}_{7.9}\text{S}_8$, which conglomerated as the results of sintering. The E_a was only calculated for the compositions $\text{Fe}_{6.15}\text{Ni}_{1.54}\text{S}_8$ and $\text{Fe}_{6.4}\text{Ni}_{1.6}\text{S}_8$.

Table 4
Comparison of the theoretical and experimental hematite weight fraction after the oxidation of *mss* achieved equilibrium

Oxidation condition	Bulk <i>mss</i> composition	Theoretical equilibrium hematite (wt.%)	Experimental equilibrium hematite (wt.%)
830 K, 1 atm.	$\text{Fe}_{7.9}\text{S}_8$	100.00	80.00
	$\text{Fe}_{2.37}\text{Ni}_{5.53}\text{S}_8$	26.97	25.25
	$\text{Fe}_{6.15}\text{Ni}_{1.54}\text{S}_8$	77.50	76.15
	$\text{Fe}_{6.4}\text{Ni}_{1.6}\text{S}_8$	77.50	76.85
850 K, 1 atm.	$\text{Fe}_{6.15}\text{Ni}_{1.54}\text{S}_8$	77.50	76.90
	$\text{Fe}_{6.4}\text{Ni}_{1.6}\text{S}_8$	77.50	76.65

The completion of iron oxidation to hematite was assumed to derive the theoretical equilibrium hematite.

In this study, the equilibrium was defined as the oxidation products vary very little even over a prolonged period of reaction. The equilibrium phase fraction was determined by averaging the value of phase fractions over the two longest oxidation periods.

Reaction extent (y) is a function of reaction time (t). The plots of y versus t for the oxidation reactions of samples $\text{Fe}_{6.15}\text{Ni}_{1.54}\text{S}_8$ (M:S = 0.96) and $\text{Fe}_{6.4}\text{Ni}_{1.6}\text{S}_8$ (M:S = 1.00) are shown in Fig. 9a. Since the S-rich sample oxidized more rapidly and achieved equilibrium within 1.5 h, we can speculate that the increasing sulfur content in *mss* accelerates the oxidation process. For the sulfur-rich sample, more sulfur atoms were vapourized and reacted with oxygen. The sulfur oxidation to SO_2 is an exothermic chemical reaction. Chamberlain and Dunn proposed that abundant evolved sulfur, reacting with oxygen at the surface of the particle, increases the

surface temperature of the particle and speeds the oxidation of iron to hematite [48]. Fig. 9b shows the time function of the reaction rate (dy/dt) for both samples (the S-rich and non-S-rich). These time functions were derived from the curves of $y \sim y(t)$ in Fig. 9a by differentiating y with respect to t . In order to show the induction stage (discussed in Section 4.1) for *mss* oxidation, the third order polynomial data fitting was used to give $y \sim y(t)$. The derivative $dy/dt \sim t$ curves in Fig. 9b show that the reaction rate increases to a maximum and then decreases to zero when the reaction approaches completion. It is worth noting that the induction stage was shown with the aid of a theoretical model. However, the experimental data in Fig. 9a only show a decelerating reaction rate due to the difficulty of data collection in a very short time frame, where the

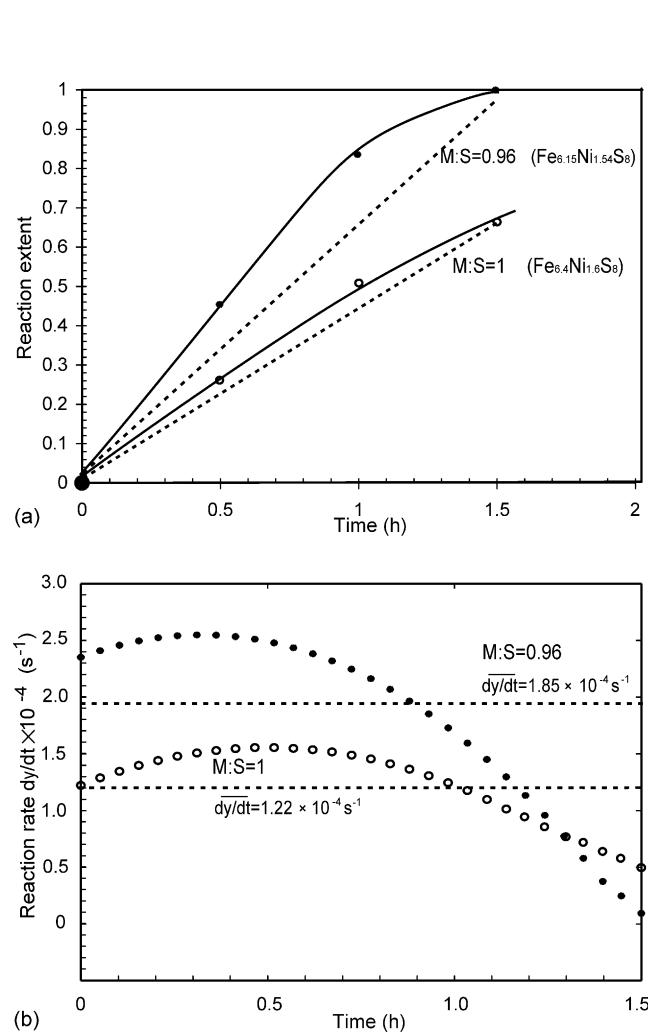


Fig. 9. (a) Progress of reaction extent with retaining time during the oxidation at 830 K for samples $\text{Fe}_{6.4}\text{Ni}_{1.6}\text{S}_8$ (M:S = 1), $\text{Fe}_{6.15}\text{Ni}_{1.54}\text{S}_8$ (M:S = 0.96). The circle symbol represents experimental data of reaction extent for the sample $\text{Fe}_{6.4}\text{Ni}_{1.6}\text{S}_8$; symbol star, for the sample $\text{Fe}_{6.15}\text{Ni}_{1.54}\text{S}_8$. The average reaction rate is derived from the slope of dashed line. (b) Dependence of reaction rate (dy/dt) on reaction time (t). The circle symbol represents calculated reaction rate for $\text{Fe}_{6.4}\text{Ni}_{1.6}\text{S}_8$; symbol of star, for $\text{Fe}_{6.15}\text{Ni}_{1.54}\text{S}_8$. The dashed line is the calculated average reaction rate over 1.5 h oxidation.

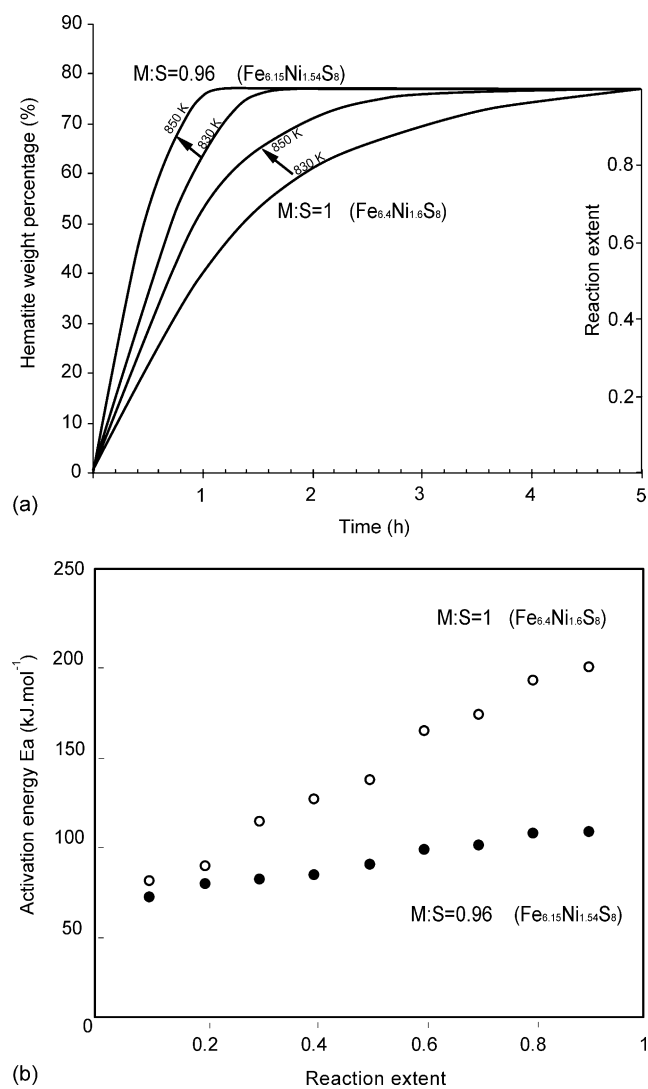


Fig. 10. (a) Graph showing the variation of hematite wt.% and reaction extent with oxidation time. The time function of hematite wt.% (or y) evolves with temperature (T). (b) Dependence of E_a on y for the oxidation of *mss* compositions $\text{Fe}_{6.4}\text{Ni}_{1.6}\text{S}_8$ and $\text{Fe}_{6.15}\text{Ni}_{1.54}\text{S}_8$ in the temperature range 830–850 K. The calculated values of activation energy are represented by symbols (○) and (●) for compositions $\text{Fe}_{6.4}\text{Ni}_{1.6}\text{S}_8$ and $\text{Fe}_{6.15}\text{Ni}_{1.54}\text{S}_8$, respectively.

induction stage occurs. It is clearly shown in Fig. 9b that the S-rich sample oxidized at a more rapid rate at the beginning and the oxidation rate approached zero after 1.5 h, whereas the non-S-rich sample was still under oxidation at a reaction rate of $5 \times 10^{-4} \text{ s}^{-1}$. The average reaction rates within 1.5 h for the samples $\text{Fe}_{6.15}\text{Ni}_{1.54}\text{S}_8$ and $\text{Fe}_{6.4}\text{Ni}_{1.6}\text{S}_8$ are 1.85×10^{-4} and $1.22 \times 10^{-4} \text{ s}^{-1}$, respectively. The activation energies for the oxidation of both compositions are calculated using Eq. (6) assuming the reaction mechanism does not change significantly in the temperature range 830–850 K. Fig. 10a shows the time dependence of hematite wt.% (or reaction extent) evolves with temperature. This time function of $y \sim y(t)$ is used to determine the E_a dependence of y (Fig. 10b). It is shown that the oxidation of $\text{Fe}_{6.4}\text{Ni}_{1.6}\text{S}_8$ has a higher E_a than $\text{Fe}_{6.15}\text{Ni}_{1.54}\text{S}_8$ over the course of reaction. The activation energy increases with y from 67.1 to 103.3 kJ mol^{-1} for *mss* composition $\text{Fe}_{6.15}\text{Ni}_{1.54}\text{S}_8$; 76.1 to 195.0 kJ mol^{-1} for $\text{Fe}_{6.4}\text{Ni}_{1.6}\text{S}_8$. The thickening of oxide layer, which inhibits the diffusion of O_2 into the unreacted *mss* particles, causes the increasing E_a with y .

The effect of nickel content on the oxidation rate of *mss* was investigated by performing oxidation experiments on two *mss* compositions $\text{Fe}_{7.9}\text{S}_8$ and $\text{Fe}_{2.37}\text{Ni}_{5.53}\text{S}_8$. The oxidation achieved equilibrium in 1 h for the nickel-rich composition and 5 h for the pure Fe *mss* sample. It appears that adding nickel to *mss* increases the oxidation rate, which reflects the fact that *mss* composition $\text{Fe}_{7.9}\text{S}_8$ requires over three times as much oxygen from the atmosphere to complete the oxidation as composition $\text{Fe}_{2.37}\text{Ni}_{5.53}\text{S}_8$ does. Oxygen diffusion into the particle is the controlling factor during oxidation of metal sulfides [11]. This reduction in the reaction rate for nickel-free *mss* is related to the high oxygen-consumption rate caused by high iron concentration, which inhibited the diffusion of oxygen into the particle. For the nickel-rich sample, on the other hand, oxygen on the surface of the particle is relatively abundant due to a lower iron concentration in *mss*.

5. Conclusions

The oxidation products of *mss* vary in our samples depending on their stoichiometry. Apart from the common oxidation products hematite and $\text{Ni}_{17}\text{S}_{18}$, mikasaite ($\text{Fe}_2(\text{SO}_4)_3$) was observed during the oxidation of $\text{Fe}_{7.9}\text{S}_8$, and pentlandite for $\text{Fe}_{6.15}\text{Ni}_{1.54}\text{S}_8$. Iron in the *mss* was preferentially oxidized to hematite, leaving a nickel enriched *mss* core. Nickel in the *mss* samples was less active than iron and eventually existed in the form of $\text{Ni}_{17}\text{S}_{18}$, a pyrrhotite-like phase. For iron–nickel *mss*, X-ray diffraction evidence shows that the *mss* gradually underwent a topotactic structural transformation from hexagonal (P6/mmc) to trigonal (P3 2) during the oxidation. The transformation was related to the enrichment of nickel in *mss*.

This study also demonstrated that increasing sulfur content in the *mss* accelerates the oxidation rate of *mss*. Also, the oxidation of *mss* samples showed a decrease in reaction rate as Ni:Fe atomic ratio decreased.

Acknowledgments

This research was supported by Australian Research Council and Australian Institute for Nuclear Science and Engineering. HW would like to thank the Australian Education, Science and Training Department for the APA award, which has allowed this work to be carried out.

References

- [1] D.J. Vaughan, J.R. Craig, *Mineral Chemistry of Metal Sulfides*, Cambridge University Press, Cambridge, 1978.
- [2] J.G. Dunn, L.C. Mackey, *J. Therm. Anal.* 39 (1993) 1255.
- [3] J.G. Dunn, V.L. Howes, *Thermochim. Acta* 282/283 (1996) 305.
- [4] A.C. Chamberlain, The effect of stoichiometry on the thermal behavior of synthetic iron–nickel sulfides, Ph.D. Dissertation, Curtin University of Technology, 1996.
- [5] A.C. Banerjee, *Indian J. Chem.* 14A (1976) 845.
- [6] Z. Asaki, K. Matsumoto, T. Tanabe, Y. Kondo, *Metall. Trans. B* 14B (1983) 109.
- [7] Z. Asaki, S. Mori, M. Ikeda, Y. Kondo, *Metall. Trans. B* 16B (1985) 627.
- [8] N.S. Saliullin, E.B. Gitis, *J. Appl. Chem. U.S.S.R.* 41 (1968) 1596.
- [9] M.J. Nichol, P.D. Scott, *J. S. Afr. Inst. Min. Metall.* (1979) 298.
- [10] R.T. Lowson, *Chem. Rev.* 5 (1982) 461.
- [11] J.G. Dunn, A.C. Chamberlain, *J. Therm. Anal.* 37 (1991) 1329.
- [12] R.V. Nicholson, *Short Course Handbook on Environmental Geochemistry of Sulfide Mine-Wastes*, Mineralogical Association of Canada, Nepean, Ont., 1994.
- [13] M.P. Janzen, R.V. Hicholson, J.M. Scharer, *Geochim. Cosmochim. Acta* 64 (2000) 1511.
- [14] G. Kullerud, Experimental techniques in dry sulfide research, in: G.C. Ulmer (Ed.), *Research Techniques for High Pressure and High Temperature*, Springer-Verlag, Berlin, 1971.
- [15] B. Etschmann, A. Pring, A. Putnis, B.A. Grguric, A. Studer, *Am. Miner.* 89 (2004) 39.
- [16] H. Wang, A. Pring, Y. Ngothai, B. O'Neill, *Geochim. Cosmochim. Acta*, in press.
- [17] WaveMetrics Inc., Igor Pro Version 4.0, WaveMetrics Inc., USA, 2000.
- [18] H.M. Rietveld, *Acta Crystallogr.* 22 (1967) 151.
- [19] H.M. Rietveld, *J. Appl. Crystallogr.* 2 (1969) 65.
- [20] E.H. Kisi, *Mater. Forum.* 18 (1994) 135–153.
- [21] R.J. Hill, C.J. Howard, *J. Appl. Crystallogr.* 18 (1985) 173.
- [22] R.J. Hill, C.J. Howard, LHPM: A Computer Program for Rietveld Analysis of X-ray and Neutron Powder Diffraction Patterns, Australian Nuclear Science and Technology Organization, 1998.
- [23] N. Alsen, *Geologiska Foereningens i Stockholm Foerhandlingar.* 47 (1925) 19.
- [24] G. Collin, C. Chavant, R. Comes, *Acta Crystallogr. B* 39 (1983) 289.
- [25] A.D. Pearson, M.J. Buerger, *Am. Miner.* 41 (1956) 804.
- [26] L. Pauling, S.B. Hendricks, *Am. Chem. Soc.* 47 (1925) 781.
- [27] P.C. Christidis, P.J. Rentzeperis, *Zeitschrift fuer Kristallographie.* 144 (1976) 341.
- [28] R.A. Yund, H.T. Hall, *J. Petrol.* 11 (1970) 381.
- [29] S. Vyazovkin, C.A. Wright, *Annu. Rev. Phys. Chem.* 48 (1997) 125.
- [30] S. Vyazovkin, *New J. Chem.* 24 (2000) 913.
- [31] S. Vyazovkin, *J. Comput. Chem.* 18 (1997) 393.
- [32] S. Vyazovkin, D. Dollimore, *J. Chem. Inf. Comput. Sci.* 36 (1996) 42.
- [33] R. Mohan, M.D. Mckinley, G.W. Douglas, *Proceedings of the Fifth Underground Coal Conversion Symposium*, Alexandria, VA, 1979.
- [34] Z. Zhang, L. Wang, Y.K. Liu, X. Feng, J. Xi, *Jian Jiaotong Univ.* 37 (2003) 11.

- [35] J.G. Dunn, L.C. Mackey, J. Therm. Anal. 37 (1991) 2143.
- [36] J.G. Dunn, G.C. De, B.H. O'Connor, *Thermochim. Acta* 145 (1989) 115.
- [37] J.G. Dunn, G.C. De, B.H. O'Connor, *Thermochim. Acta* 155 (1989) 135.
- [38] F.R.A. Jorgensen, F.J. Moyle, J. Therm. Anal. 25 (1982) 473.
- [39] F.R.A. Jorgensen, F.J. Moyle, J. Therm. Anal. 29 (1984) 13.
- [40] F. Habashi, *Chalcopyrite: its Chemistry and Metallurgy*, McGraw Hill International Book Co., New York, 1987.
- [41] F.T. Bumazhnov, A.S. Lenchev, *Dokl. Aolg. Akad. Nauk.* 25 (1972) 953.
- [42] H. Tsukada, Z. Asaki, T. Tanabe, Y. Kondo, *Metall. Trans. B* 12B (1981) 603.
- [43] T. Rosenqvist, *J. Iron Steel Inst.* 176 (1954) 37.
- [44] M. Nagamor, M. Kameda, *Trans. Jpn. Inst. Met.* 19 (1968) 187.
- [45] E.T. Turkdogan, *Trans. TMS-AIME* 242 (1968) 1665.
- [46] A.V. Vanyukov, Y.B. Boitkovskii, *Zh. Prikl. Khim.* 51 (1978) 1124.
- [47] J.G. Dunn, *Thermochim. Acta* 300 (1997) 127.
- [48] A.C. Chamberlain, J.G. Dunn, *Thermochim. Acta* 340/341 (1999) 367.
- [49] G. Kullerud, *Can. Miner.* 7 (1962) 353.
- [50] H. Wang, Y. Ngothai, B. O'Neill, A. Pring, The Effects of S Fugacity on the Exsolution of Pentlandite (Fe, Ni)₉S₈ from the Monosulfide Solid Solution (Fe, Ni)S, in: *Proceedings of the 31st Annual Australian Chemical Engineering Conference*, Adelaide, Australia, 2003.
- [51] K.C. Misra, M.E. Fleet, *Econ. Geol.* 68 (1973) 518.